Word Count: 3757

Revision 4

Mushroom-shaped Growth of Crystals on the Moon

JIAXIN XI[1,2,3]†, YIPING YANG[1,3]†, HONGPING HE[1,2,3*], HAIYANG XIAN[1,3], SHAN LI[1,2,3], XIAOJU LIN[1,3], JIANXI ZHU[1,2,3], H. HENRY TENG[4]

[1]CAS Key Laboratory of Mineralogy and Metallogeny/Guangdong Provincial Key Laboratory of Mineral Physics and Materials, Guangzhou Institute of Geochemistry, Chinese Academy of Sciences, Guangzhou, China.

[2]University of Chinese Academy of Sciences, Beijing, China.

[3]CAS Center for Excellence in Deep Earth Science, Guangzhou, China.

[4]Institute of Surface-Earth System Science, School of Earth System Science, Tianjin University, Tianjin 300072, China

Corresponding author: hehp@gig.ac.cn

†These authors contributed equally to this work: Jiaxin Xi, Yiping Yang.

ABSTRACT

Advances in crystal nucleation and growth over the past three decades have led to the understanding that crystallization proceeds through a variety of pathways, ranging from the conventional atom-by-atom model to the particle aggregation- or amorphous transformation-based non-classical modes. Here, we present a novel mineralization mechanism exemplified by a lunar chromite formed via solid-liquid interface reactions, through investigations towards a lunar breccia returned by the Chang'e 5 mission. The chromite occurs in the middle of a whisker-shaped intergrowth structure made by olivine at the bottom and nanospheres of troilite and metallic iron at the top. Morphological observation and size statistics of the nanospheres, including those within the whisker structure and the others dispersed in glass, suggest the nanophases attached to olivine with coherent crystallographic orientations, possibly through an oriented aggregation process. The chromium deficiency in the olivine near the interface between olivine and chromite suggests that Cr in chromite originated from olivine, but the significantly reduced ferrous concentration in the glass surrounding chromite indicates the iron was derived from surrounding impact-induced glass. Based on laboratory observations and simulated calculations of energy and lattice mismatch, we propose that chromite crystallized at the interface between troilite and olivine in the impact melts, during which the nanospheres were lifted up and transported away from olivine surface and form a mushroom-shaped structure. This finding suggests that oriented attachment growth, chiefly confined to homogeneous systems thus far, can also take place in

heterogeneous systems far from equilibrium, such as that produced by the impacts. It is conceivable that the studied crystallization pathway occurring on the heterogeneous interfaces may have been a common mineralization mode at highly-nonequilibrium conditions.

Keywords: Chang'e 5 lunar regolith; whisker growth; nanoparticles; nonequilibrium crystallization; impact melt; chromite

INTRODUCTION

Crystallization is a material attribute of condensed substances (Penn and Banfield 1998; Banfield et al. 2000; De Yoreo et al. 2015; He et al. 2021). The understanding of geological processes, materials science, and biogeochemistry heavily relies on the advances of crystallography and crystal chemistry (Ivanov et al. 2014; De Yoreo et al. 2015). In the last decades, a wide range of growth mechanisms concerning the mineralization of oxides, silicates, carbonates, metals, organic compounds, and biominerals in natural and synthetic systems have been reported (Burton 1951; Kashchiev 2003; Cantaert et al. 2012; Lenders et al. 2014; Nielsen et al. 2014). These studies summarized the classical theories, i.e., step growth and Ostwald ripening (Petsev et al. 2003; Giuffre et al. 2013), and non-classical pathways such as crystallization by particle attachment (CPA) (De Yoreo et al. 2015). Classical theories describe the incorporation of individual ions or molecules onto high-energy crystal faces (Baronnet 1972). Although proven to be operative for homogeneous crystallization of many materials in dilute solutions (Ivanov et al. 2014), the classical

model fails to predict the nonequilibrium crystallization of supercooled liquids of metallic alloys (Hu and Tanaka 2022) and micro/nanoparticles with atypical habits under high supersaturation (Li et al. 2013). Instead, laboratory and field observations have revealed the attachment of particles with sizes ranging from multi-ion complexes to fully-formed nanoparticles (Lee et al. 2016), a mechanism commonly referred to as a non-classic growth pathway. Oriented attachment (OA), a key step of CPA, mainly involves aggregating nanocrystals in homogeneous systems to self-assemble into extended structures on specific crystal planes (De Yoreo et al. 2015; He et al. 2021).

However, under extreme disequilibrium conditions (e.g., meteorite impact), crystal growth pathways may be much more complicated. This is because extreme nonequilibrium crystallization may involve some uncommon processes, such as the rapid growth of minerals, the generation of new phases, the complex ion exchange between different phases (Hauwiller et al. 2018) and so on. These process are allowed by the rapid change of supersaturation and partition coefficient between the crystallines and melts (Sunagawa 2005; Feng et al. 2009). and have rarely been considered in existing crystal growth theories. Related processes and mechanisms need to be explored to expand the current knowledge base and to predict minerals evolution in extreme conditions.

In this study, we investigated in detail the growth mechanism in the lunar breccia glass returned by China's Chang'e-5 (CE5) mission, and report a novel mineral growth pathway taking place under a far-from-equilibrium condition. The work describes whisker crystallization between two attached (nano)crystal phases, wherein the

pre-existing crystals and matrix provide elements for the newly-formed phase, resulting in the formation of a parallel intergrowth of olivine, chromite, troilite, and nano-phase metallic iron ($npFe^0$) spheres. This finding may provide a diagnostic mineral assemblage and texture for impact-induced nonequilibrium growth and shed light on the further interpretations of crystal growth under extremely-nonequilibrium environments.

SAMPLE AND METHODS

The lunar regolith sample (CE5C0000YJYX125) used in this study was returned by the Chang'e-5 mission from Oceanus Procellarum region of the Moon, and provided by the China National Space Administration (CNSA). The studied particles were selected from a breccia clast in a Mikrouna glove box (N_2 > 99.999%, H_2O < 0.01 ppm, O_2 < 1.0 ppm). Selected samples were embedded in epoxy resin and then polished for further investigations.

Scanning electron microscope (SEM) observations. SEM observations were conducted with a TESCAN MIRA3 field-emission scanning electron microscope operated at a voltage of 20 kV after the surface of the sample was coated by carbon.

Electron Probe X-ray Microanalyzer (EPMA) analyses. The elemental composition of minerals was determined on a JEOL JXA-8230 (Tokyo, Japan) electron probe microanalyzer at operating conditions of 15 kV, 20 nA, and ~3 μm beam diameter. The ZAF correction method was used for data reduction, with all the standard metals/minerals are produced by Structure Probe, Inc (SPI) Supplies (United

States).

Focused-ion-beam (FIB) cutting and transmission electron microscopy (TEM) observations. An FEI Scios dual-beam system was used for the FIB cutting on the silicon wafer sample. After being located and deposited with Pt, thin sections (with a thickness of ~ 100 nm) of interested area for TEM observations were then cut by Ga^+ ion beam in the FIB system. Then the observation in both TEM and scanning TEM (STEM) modes was performed using an FEI Talos F200S TEM at a accelerating voltage of 200 kV. Energy dispersive spectroscopy (EDS) mapping were performed in STEM mode with two superX detectors, with a dwell time of 10 μs and the results summed from 50 frames. Energy dispersive spectroscopy (EDS) semi-quantitative analyses from mapping data were conducted using the FEI Velox software. Electron energy loss spectroscopic (EELS) analyses were performed in STEM mode with a Gatan 1077 EELS spectrometer. EELS results were acquired in a dual mode with zero-peak locking. Spectroscopic images have a pixel step of 2 nm. All the EELS data processing tasks (including background and plural scattering subduction, signal integration, data fitting, and mapping) were conducted in the Gatan Microscope Suite (GMS) software (version 3.50).

Calculation of $Fe^{3+}/\sum Fe$ ratios. According to EELS quantitative studies (van Aken et al. 1998; van Aken and Liebscher 2002), the integral intensity ratio of $I(L_3)/I(L_2)$ computed from two 2.1 eV-width windows (i.e., 708.85–710.95 and 719.65–721.75 eV) depends on the ferric iron percentage, i.e., $Fe^{3+}/\sum Fe$. The calculated integral $I(L_3)/I(L_2)$ rations were then converted to $Fe^{3+}/\sum Fe$ ratios through

130 the equation (van Aken and Liebscher 2002):

131 $$\frac{I(L_3)}{I(L_2)} = \frac{1}{a \cdot x^2 + b \cdot x + c} - 1,$$

132 where x is the ferric iron concentration, $Fe^{3+}/\sum Fe$. The parameters a, b, and c are
133 equal to 0.193±0.007, -0.465±0.009, and 0.366±0.003, respectively. The statistical
134 standard deviation of the $I(L_3)/I(L_2)$ values is less than 5%, and the absolute
135 systematic errors for quantitative determination are roughly 0.05 for $Fe^{3+}/\sum Fe < 0.4$
136 and 0.03 for $Fe^{3+}/\sum Fe > 0.6$. Then the results were used to map the $Fe^{3+}/\sum Fe$ ratios of
137 specific regions, via applying pseudo color to characterize the quotient of EELS
138 signal integral in the two windows of 708.85–710.95 and 719.65–721.75 eV. The
139 maps of $Fe^{3+}/\sum Fe$ ratios with pseudo color were also produced by the ratio of
140 $I(L_3)/I(L_2)$ in every single EELS spectrum within the mapping area. According to
141 previous calculation, the $I(L_3)/(L_2)$ lower than 1.7 represents an absence of Fe^{3+} (i.e.,
142 all the Fe species are identified as metallic Fe and/or Fe^{2+}), while the $I(L_3)/(L_2)$ higher
143 than this value indicates an existence of Fe^{3+} with various proportions in the sample
144 (van Aken and Liebscher 2002).

145

146 # RESULTS

147 ## Morphological observations

148 The collected CE5 breccia sample is composed of several clasts that are
149 cemented by impact melt (Fig. 1A and Fig. S1A). A unique texture of the rock is a
150 stripe-like pattern of parallel olivine rods (Figs. 1B and S1) situated in the glass

matrix. Whisker-shaped nano-needles with multiple phases spout perpendicular to the olivine base to form 'mushrooms' with chromite as stems and $npFe^0$ sitting in troilite as caps (Figs. 1C and D). Olivine particles are uniformly oriented to form columns and share their [100] zone axis with the [001] of chromite (Figs. 2A-C, and fast Fourier transform patterns in Figs. 2D-E). The conically-shaped chromite crystals, with a diameter of ~ 40 nm at the bottom and ~ 20 nm at the top, protrude from the olivine base (Figs. 2A-C). Nanospheres of metallic iron (i.e., $npFe^0$) usually occur at the top of the whisker structure, with troilite located between $npFe^0$ and chromite crystal (Fig. 2C). Troilite connects $npFe^0$ and chromite by sharing its [110] zone axis with the [001] zone axis of $npFe^0$ and the [110] zone axis of chromite simultaneously (Fig. 2). Nanospheres of $npFe^0$ and troilite are adjacent on the top of each chromite needle (Figs. 2A-C). Besides being a part of the whisker structures, most (~ 89%) nanospheres of troilite and $npFe^0$ are irregularly distributed in the glass (Fig. 2A). These $npFe^0$ and troilite nanospheres in glass have a similar size to those in the whisker structures (Fig. 3), with diameters in the range of 24.3 ~ 31.6 nm.

Chemical analyses

Energy-dispersive spectroscopy (EDS) (Fig. S1 and Table 1) and electron energy loss spectroscopy (EELS) integrated with transmission electron microscopy (TEM) (Fig. 4 and Table 2) reveal a complex distribution of iron species. Note that the EDS quantification and EELS results of nanoparticles, including troilite, $npFe^0$ and chromite whiskers, inevitably have a contribution of silicate glass (Table 1 and Fig. 4). Olivine crystals have a Fe content ranging from 8.9 at% to 11.0 at%, with an average

chemical formula of $(Mg_{1.00}Fe_{0.74}Ti_{0.09}Cr_{0.02}Al_{0.02}Mn_{0.01})_{\sum=1.88}SiO_4$ (Fo=57). Metallic iron occurs exclusively in the $npFe^0$ nanospheres, whereas Fe^{2+} is dominant in olivine, chromite, and troilite (Table 2 and Figs. 4B-D). The small account of Fe^{3+} in $npFe^0$ and nanophase troilite shown by EELS maps in Fig. 4 is contributed by surrounding Fe^{3+}-bearing glass, as a result of the spherical shape of these nanoparticles wrapped by glass in the FIB section. In the meantime, the valence state and distribution pattern of the Fe ions in the glass are different from the crystalline phases within the whisker structure. For glass located with unequal distance to the whisker structure, the different position and shape of the Fe $L_{2,3}$-edge in EELS spectra present a mixture of ferric and ferrous iron with variable ratios (Table 2 and Fig. 4C) (Garvie and Buseck 1998; van Aken et al. 1998; van Aken and Liebscher 2002). EELS results (Figs. 4B-D) reveal an increase of $Fe^{3+}/\sum Fe$ in the glass around chromite needles (Glass A) compared to the peripheral glass (Glass B), which is indicated by the rightward shift of the Fe $L_{2,3}$-edge position and a higher basic intensity of the Fe L_3-edge of Glass-A (van Aken and Liebscher 2002).

The occurrence of Cr in chromite, olivine and glass is confirmed by EELS spectra (Fig. S2), of which Cr-bearing olivine has been documented as a product of high temperature crystallization (Chen et al. 2022). Note that in the olivine particles connected with whisker structures, Cr occurs unevenly with a lower content (~ 0.09 at%) at the edge and a higher content (~ 0.26 at%) in the interior region (Fig. 5). On the contrary, the olivine particles embedded in the glass (without any connection with chromite) display uniform Cr distribution.

DISCUSSION

The chemical and structural analyses suggest that the intergrowth structure of chromite, troilite, and $npFe^0$ attached to the olivine may have evolved in three stages: (1) the formation of $npFe^0$ and troilite nanospheres (Figs. 6A-C), (2) the oriented attachment between nanospheres and olivine (Figs. 6D and E), and (3) the growth of chromite (Figs. 6F and G).

Formation of $npFe^0$ nanospheres

$NpFe^0$ is a common product of (micro)meteoroid impact (Hapke et al. 1975; 2001; Christoffersen et al. 1996; Keller and McKAY 1997; Xian et al. 2023) and solar wind irradiation (Housley et al. 1974; Hapke et al. 2001; Badyukov 2020). In this study, the striped texture observed in the section, being composed of olivine and glass platelets (or tabular grains) in three dimensions, is comparable to barred olivine presenting in some chondrules (Weisberg 1987; Tsuchiyama et al. 2004). The impact origin of $npFe^0$ is further indicated by the disproportionation reaction of ferrous iron (Xian et al. 2023), which is suggested by the complexly spatial coexistence of $npFe^0$, Fe^{2+} and Fe^{3+}. Especially, the decrease of Fe^{3+} content in glass with increasing distance to the whisker structure also supports the occurrence of disproportionation reaction (Fig. 4C). Another common product of impacts, i.e., troilite, have been reported and studied by numerous studies of extraterrestrial sample, including meteorites and lunar regolith samples (e.g., Tomkins 2009; Guo et al. 2022). Spherical inclusions of troilite and troilite-metal (usually troilite-iron) complex in

217 silicate glass are demonstrated to be related to a high temperature and high cooling
218 rate that help with driving some of sulfur out of the initially mental sulfide phases as:
219 $Fe_{1-x} \rightarrow FeS(troilite) + xS_2(gaseous\ sulfur)$ (Lauretta et al. 1997; Tomkins 2009). The
220 impacts generate metallic iron, ferric iron and troilite ± iron in the melt which was
221 dominated by ferrous iron (Mayne et al., 2009). The size of $npFe^0$ and troilite-iron
222 nanoparticles provide an estimation of the reaction temperature (Nanda et al. 2002;
223 Xian et al. 2023). Calculation shows that with a number density of ~ 6.7 per μm^2 and
224 an average diameter of ~ 26.2 nm, the nanoparticles form at a temperature higher than
225 1500 °C, which is corresponded to a (semi-)liquid condition. The liquid environment
226 of impact-induced melts facilitates the nonequilibrium crystallization of the new
227 mineral phase (De Yoreo et al. 2015; Ivanov et al. 2014; He et al. 2021), i.e.,
228 chromite.

229 **Oriented attachment between nanospheres and olivine**

230 Oriented attachment (OA) has been found chiefly responsible for the
231 development of certain specific morphological features such as dendrites and
232 whiskers, by creating coherent interphase boundaries for primary particles to
233 assemble and form branches (Li et al. 2013; De Yoreo et al. 2015; Lu et al. 2006).
234 The chromite needles with nanospheres of troilite and $npFe^0$ on the olivine surfaces
235 may be interpreted within the framework of modern nonequilibrium growth processes
236 by three possible pathways:

237 (1) *OA occurs in the space between chromite and olivine, and that between*
238 *nanospheres and chromite.* This suggests that the chromite branches and nanospheres

of troilite and $npFe^0$ crystallize independently at the early stage, followed by the assembly of them with olivine.

(2) *OA only occurs between nanospheres and chromite*, while the chromite crystallized under an environment far from equilibrium conditions and crystallized from the melt before the attachment of the nanospheres.

(3) *OA does not occur*; in such a case, chromite and nanospheres within the whisker structure are both accessory minerals of olivine crystallization.

However, the first two hypotheses lead to the possibility to form isolated chromite branches instead of being associated with any nanosphere, contradicting our observations that chromite only occurs within the whisker structure. The absence of isolated chromite branches without any connection with troilite and $npFe^0$ spheres suggests that the chromite formation is intertwined with the growth of the nanospheres. The third hypothesis fails to interpret the wide distribution of troilite and $npFe^0$ nanospheres in the glass, particularly because all the nanospheres have a similar size (Fig. 3). Thus, there appears to exist additional pathways responsible for the formation of the whisker structure.

Our observations that chromite branches are always covered by troilite or troilite-iron nanospheres (Fig. 6) imply the formation of chromite needles was later than nanospheres, i.e., after attachment of nanospheres to olivine. More importantly, our observations suggest that OA can also occur in an heteroepitaxial fashion between different species, though most related studies have focused on the assembly of co-aligned nanocrystals of the same mineral species (De Yoreo et al. 2015).

Crystallization of chromite

The decrease of Cr in the olivine particles attached to chromite in conjunction with the uniform distribution of Cr in isolated olivine crystals suggests that olivine may be one of the chemical sources of Cr for chromite. Olivine with high Cr content can be formed under high temperature and pressure conditions (Burns 1975; Chen et al. 2022). But the incompatibility of Cr in the olivine drives it to migrate from the olivine lattice to reduce the total Gibbs free energy, leading to an increase of the partition coefficients of Cr between the melt and olivine (Min 1992; Sunagawa 2005; Chen et al. 2022). When the melt becomes supersaturated relative to Cr, chromite nucleates from the melt (e.g., Arai 1978) and firstly crystallizes at the high-energy defect plane formed by the attachment between olivine and nanospheres. The growth of chromite creates a chemical potential gradient driving more Cr cations losing from the olivine at high temperatures, which causes the apparent lower Cr contents adjacent to the chromite grains here.

From the crystallographic perspective, the occurrence of chromite between troilite and olivine can be interpreted by using the degree of lattice mismatch between the two adjacent phases. The lattice mismatch (Δ) is expressed as:

$$\Delta = \frac{a_s - a_e}{a_s}, \quad (1)$$

where a_s and a_e are the original lattice constants of the primary crystal and the overgrowth material, respectively. Low mismatch, i.e., close resemblance of crystal structures, leads to an easier intergrowth (Liu and Zhang 2020). Using relevant cell parameters (Table 3), the lattice mismatch between olivine and $npFe^0$ (Δ_1) is:

283 $$\Delta_1 = \frac{a_s - a_e}{a_s} = \sqrt{\left|\frac{a_{oli\text{-}a} - a_{Fe}}{a_{oli\text{-}a}}\right| \cdot \left|\frac{a_{oli\text{-}b} - a_{Fe}}{a_{oli\text{-}b}}\right|} = 0.99;$$

284 the lattice mismatch between olivine and troilite (Δ_2) is:

285 $$\Delta_2 = \frac{a_s - a_e}{a_s} = \sqrt{\left|\frac{a_{oli\text{-}a} - a_{FeS}}{a_{oli\text{-}a}}\right| \cdot \left|\frac{a_{oli\text{-}b} - a_{FeS}}{a_{oli\text{-}b}}\right|} = 0.27.$$

286 In the case of the lattice mismatch between olivine and chromite, the *a* of
287 chromite is an integral multiple of the *a* of olivine, which leads to a significant
288 decrease of their lattice mismatch (Δ_3). Thus, the calculation can be simplified as:

289 $$\Delta_3 = \frac{a_s - a_e}{a_s} \approx \frac{a_{oli\text{-}b} - a_{Chr}}{a_{oli\text{-}b}} = 0.20.$$

290 Calculation results show that the lattice mismatch between olivine and npFe^0 (Δ_1
291 = 0.99) is much higher than that between olivine and troilite (Δ_2 = 0.27). This means
292 that the attachment of troilite to olivine (along the $(1\bar{1}0)$ plane of olivine as determined
293 by orientation in Fig. 2 and S3) can occur more readily readily than that of npFe^0 to
294 olivine. Note that, for the growth of chromite on olivine, the cell parameter *a* for
295 chromite is exactly an integral multiple of that for olivine (Table 3), resulting in a
296 lower lattice mismatch ($\Delta_3 \approx 0.20$). Based on the lattice mismatch values between the
297 three mineral phases and olivine, one can predict that chromite has the strongest
298 tendency to attach to olivine in the studied sample, followed by troilite, while npFe^0 is
299 relatively more difficult. This order is supported by the excellent match between the
300 oxygen sublattices of olivine and spinel phases (chromite, magnetite) established by
301 previous studies (e.g. Champness 1970), and also fits consistently with the mineral
302 assemblage in the whisker structures observed here.

303 Nano-needles made of olivine, chromite, troilite and npFe^0 in the elongation
304 direction are ubiquitous (Figs. 1C and D) although those of olivine and troilite alone
305 can be occasionally observed (Figs. 6E and F). However, an exclusive association
306 between olivine and npFe^0 has never been observed. TEM observations suggest that
307 crystallization of chromite only took place after successful attachment of troilite to
308 olivine.

309 **Mineral growth pathway and formation of novel whisker structure**

310 We propose a new non-classical growth pathway that can explain chromite
311 crystallization from the primary impacted melting system with the elemental
312 contributions of the melt and crystallized olivine. In this case, new minerals springing
313 from early-cystallized mineral's surface, extracting elements from the neighboring
314 crystals and melt. Such a pathway is further supported by a simulation of energy
315 balance. For a rapidly cooling system that far from equilibrium, the interaction energy
316 can be simplified as the total work of electrostatic force and the van der Waals force
317 (Penn 2004). Here the evolution of interface energy on the interface between
318 troilite-iron nanospheres and olivine during the oriented attachment was estimated,
319 applying the DLVO (Derjaguin, Landau, Verwey, and Overbeek) theory and the
320 Fuoss equation (Turnbull 1956; Stokes and Evans 1997) via considering the minerals
321 as electrolyte particles in the melts (liquid) at a high temperature and pressure
322 condition:

323 $$V_T(h) = \pi r\left(\frac{-A}{12\pi H} + \frac{64ckT\Gamma_o^2 e^{-\kappa H}}{\kappa^2}\right), \quad (1)$$

324 where

This is the peer-reviewed, final accepted version for American Mineralogist, published by the Mineralogical Society of America.
The published version is subject to change. Cite as Authors (Year) Title. American Mineralogist, in press.
DOI: https://doi.org/10.2138/am-2023-9214. http://www.minsocam.org/

325 $$\frac{1}{\kappa} = \frac{\varepsilon_r \varepsilon_0 kT}{2000 e^2 N_A I}, \qquad (2)$$

326 and

327 $$\Gamma_o = \frac{\exp(ze\Phi_o / 2kT) - 1}{\exp(ze\Phi_o / 2kT) + 1}. \qquad (3)$$

328 In these equations, $V_T(h)$ is the total interaction energy, r the radius of the
329 particle, A the Hamaker constant, H the separation distance between particles (meters),
330 c the bulk concentration of electrolyte, κ is the reciprocal of the Debye length
331 (meters^{-1}). Other common parameters are denoted by k (Boltzmann's constant), T
332 (temperature), ε_r (dielectric constant of the medium), ε_0 (the vacuum permittivity), N_A
333 (Avogadro's number), ze (charge on the electrolyte ions), and Φ_o (surface potential in
334 volts). The Hamaker constant (A) is defined by：

335 $$V_A = -\frac{AR}{12H}; \qquad (4)$$

336 and V_A=-GMm/H. (5)

337 with V_A is the gravitational potential energy, G is the gravitational constant, M and m
338 represent the mass of the two particles, and H is the distance between the two objects.
339 The $V_T(h)$ in this study is estimated to be ~ 5.41×10^{-4} kJ/mol ($\Delta G1$ in Fig. 7) for the
340 attachment of a troilite nanoparticle to olivine. After OA, chromite starts to appear on
341 the interface. The growth rate of nano-phase crystallization in an interface-controlled
342 polymorphic phase transformation is given by:

343 $$x=k_0 T \exp(-Q/RT)[1-\exp(-\Delta G_r/RT)], \qquad (6)$$

where k_0 is a constant, Q is the activation energy for growth, ΔG_r is the free energy change of reaction, and R is the gas constant (Turnbull 1956; Rubie et al. 1990). Therefore, the ΔG_r can be derived from equation (6) as:

$$\Delta G_r = -RT \cdot \ln[1 - \frac{x}{k_0 T \exp(-Q/RT)}]. \quad (7)$$

The activation energy for the chromite growth was calculated to be 6.88×10^{-5} kJ/mol ($\Delta G2$). This value is much lower than the total energy produced by the attachment of troilite to olivine, an indication that that chromite crystallization can readily take place on the surface of olivine (i.e., the interface between troilite and olivine). According to the calculations of both lattice mismatch degree and interface energy, OA between the troilite-iron nanoparticles and olivine generates an unstable interface with a high lattice mismatch degree and a high interface energy, which facilitates the nucleation of chromite on the interface to decrease the lattice mismatch degree and interface energy (Fig. 7). Thus, the crystallization of chromite on the interface between the olivine and troilite-iron nanoparticles is advantageous for stabilizing the interface between the two, until the activation energy required for further crystallization cannot be provided.

IMPLICATION

Via detailed textural and compositional analysis of a mushroom-shaped structure from the CE5 lunar breccia, we describe a newly-formed chromite occurring on olivine base and capped by nanospheres of troilite and $npFe^0$ (Fig. S4). The whisker growth of chromite was induced by the occurrence of oriented attachment and the

366 nucleation of chromite from Cr-supersaturated melt, and was fed by olivine for Cr and
367 melt for Cr and Fe. We propose a novel non-classical growth pathway to create new
368 mineral phases on the heterogeneous interfaces between primary minerals,
369 incorporating impurity ions of neighboring minerals. We reveal that except in
370 single-phase crystal systems, OA could also operate in multi-phases crystallization
371 system.

372 The previously unrecognized crystal-growth pathway that forming a
373 mushroom-shaped integrowth of olivine, chromite and (troilite-iron) nanospheres
374 responsible for the formation of whisker structure containing different mineral phases
375 requires extreme nonequilibrium conditions. Given the frequent (micro)meteoroid
376 impacts on the Moon, we suspect this mechanism is likely to be wide-spread in lunar
377 regolith and thus may be an indicator for the extreme unequilibrium crystallization.
378 The mechanism may provide new insights for the local mineralogy on the Moon, and
379 for further interpretations of crystallization at highly-unequilibrium environments.
380 The observed whisker structure has until now never been reported in earth samples,
381 though whiskers and dendrites of mantle-derived minerals (e.g., pyroxene and olivine)
382 are common in glass-rich igneous rock such as obsidian (Welsch et al. 2014). The
383 temperature, pressure and other geochemical conditions acquired by the occurrence of
384 this mechanism still need more detailed experiments to explore.
385

Acknowledgements

We thank all the team members of China's Chang'e Lunar Exploration Project for their hard work in returning lunar samples and CNSA for providing the lunar sample CE5C0000YJYX125. This work was financially supported by the National Natural Science Foundation of China (Grant Nos. 41921003 and 42202039),Youth Innovation Promotion Association CAS (Grant No. 2021353), Funding by Science and Technology Projects in Guangzhou (202201010385) and Science and Technology Planning Project of Guangdong Province, China (2023B1212060048).

REFERENCES

Arai, S. (1978) Chromium spinel lamellae in olivine from the Iwannai-Dake peridotite mass, Hokkaido, Japan. Earth & Planetary Science Letters, 39, 267–273.

Badyukov, D.D. (2020) Micrometeoroids: the flux on the Moon and a source of volatiles. Solar System Research, 54, 263–274.

Banfield, J.F., Welch, S.A., Zhang, H., Ebert, T.T., and Penn, R. L. (2000) Aggregation-based crystal growth and microstructure development in natural iron oxyhydroxide biomineralization products. Science, 289, 751–754.

Baronnet, A. (1972) Growth mechanisms and polytypism in synthetic hydroxyl-bearing phlogopite. American Mineralogist, 57, 1272–1293.

Burns, R.G. (1975) On the occurrence and stability of divalent chromium in olivines included in diamonds. Contributions to Mineralogy and Petrology, 51, 213–221.

Burton, W.K., Cabrera, N., and Frank, F.C. (1951) The growth of crystals and the equilibrium structure of their surfaces. Philosophical Transactions of the Royal Society A, 243, 299–358.

Cantaert, B., Kim, Y., Ludwig, H., Nudelman, F., Sommerdijk, N.A.J.M., and Meldrum, F.C. (2012) Think positive: Phase separation enables a positively charged additive to induce dramatic changes in calcium carbonate morphology. Advanced Functional Materials, 22, 907–915.

Champness, P.E. (1970) Nucleation and growth of iron oxides in olivines, $(Mg,Fe)_2SiO_4$. Mineralogical Magazine, 37, 790–800.

Chen, S., Ni, P., Zhang, Y.X., and Gagnon, J. (2022) Trace element partitioning between olivine and melt in lunar basalts. American Mineralogist, 107, 1519–153.

Christoffersen, R., McKAY, D.S., and Keller, L.P. (1996) Microstructure, chemistry, and origin of grain rims on ilmenite from the lunar soil finest fraction. Meteoritics and Planetary Science, 31, 835–848.

De Yoreo, J.J., Gilbert, P.U.P.A., Sommerdijk, N.A.J.M., Penn, R.L., Whitelam, S., Joester, D., Zhang, H.Z., Rimer, J.D., Navrotsky, A., Banfield, J.F., Wallace, A.F., Michel, F.M., Meldrum, F.C., Colfen, H., and Dove, P.M. (2015) Crystallization by particle attachment in synthetic, biogenic, and geologic environments. Science, 349, 6760.

Feng, Y., Tianyi, M.A., and Liu, L.A. (2009) Insights into shape control and growth mechanism of inorganic nanocrystals. Science in China, 39, 864–886.

Garvie, L.A.J., and Buseck, P.R. (1998) Ratios of ferrous to ferric iron from nanometre-sized areas in minerals. Nature, 396, 667–670.

Giuffre, A.J., Hamm, L. M., Han, N., De Yoreo, J.J. and Dove, P.M. (2013) Polysaccharide chemistry regulates kinetics of calcite nucleation through competition of interfacial energies. Proceedings of the National Academy of Sciences of the U.S.A., 110, 9261–9266.

Guo, Z., Li, C., Li, Y., Wen, Y.Y., Wu, Y.X., Jia, B.J., Tai, K.R., Zeng, X.J., Li, X.Y., Liu, J.Z., and Ouyang, Z.Y. (2022) Sub-microscopic magnetite and metallic iron particles formed by eutectic reaction in Chang'E-5 lunar soil. Nature Communications, 23, 7177.

Hapke, B. (2001) Space weathering from Mercury to the asteroid belt. Journal of Geophysical Research, 106, 10039–10073.

438 Hapke, B., Cassidy, W., and Wells, E. (1975) Effects of vapor-phase deposition processes on
439 the optical, chemical, and magnetic properties of the lunar regolith. The Moon. 13, 339–
440 353.

441 Hauwiller, Matthew, R., Zhang, X.W. Liang, W.I., Chiu, C.H., Zhang, Q ., Zheng, W.J.,
442 Ophus, C., Chan, E.M., Czarnik, C., Pan, M., Ross, F.M., Wu, W.W., Chu, Y.H., Asta,
443 M., Voorhees, P.W., Alivisatos, A.P., and Zheng, H.M. (2018) Dynamics of nanoscale
444 dendrite formation in solution growth revealed through in situ liquid cell electron
445 microscopy. Nano Letters, 18, 6427–6433.

446 He, H.P., Yang, Y.P., Ma, L.Y., Su, X.L., Xian, H.Y., Zhu, J.X., Teng, H., and Guggenheim,
447 S. (2021) Evidence for a two-stage particle attachment mechanism for phyllosilicate
448 crystallization in geological processes. American Mineralogist, 106, 983–993.

449 Housley, R.M., Cirlin, E.H., Paton, N.E. and Goldberg, I.B. (1974) Solar wind and
450 micrometeorite alteration of the lunar regolith. Lunar and Planetary Science Conference
451 Proceedings, 3, 2623–2642.

452 Hu, Y.C., and Tanaka, H. (2022) Revealing the role of liquid preordering in crystallisation of
453 supercooled liquids. Nature Communications, 13, 4519.

454 Ivanov, V.K., Fedorov, P.P., Baranchikov, A.Y., and Osiko, V.V. (2014) Oriented attachment
455 of particles: 100 years of investigations of non-classical crystal growth. Russian
456 Chemical Reviews, 83, 1204–1222.

457 Kashchiev, D. (2003) Thermodynamically consistent description of the work to form a
458 nucleus of any size. Journal of Chemical Physics, 118, 1837–1851.

459 Keller, L.P., and McKAY, D.S. (1997) The nature and origin of rims on lunar soil grains.
460 Geochimica et Cosmochimica Acta, 61, 2331–2341.

461 Lauretta D.S., Lodders K., Fegley B.J., and Kremser D.T. (1997) The origin of
462 sulfide-rimmed metal grains in ordinary chondrites. Earth & Planetary Science Letters,
463 151, 289–301.

464 Lee, J., Yang, J.W., Kwon, S.G. and Hyeon, T.W. (2016) Nonclassical nucleation and growth
465 of inorganic nanoparticles. Nature Reviews, 1, 1–16.

466 Lenders, J.J.M., Altan, C.L., Bomans, P.H.H., Arakaki, A., Seyda, B., Gijsbertus, D., and
467 Sommerdijk, N.A.J.M.(2014) A bioinspired coprecipitation method for the controlled
468 synthesis of magnetite nanoparticles. Crystal Growth and Design, 14, 5561–5568.

469 Li, D.S., Soberanis, F., Fu, J., Hou, W.T., Wu, J.Z., and Kisailus, D. (2013) Growth
470 mechanism of highly branched titanium dioxide nanowires via oriented attachment.
471 Crystal Growth and Design, 13, 422–428.

472 Liu, J., and Zhang, J. (2020) Nanointerface chemistry: lattice-mismatch-directed synthesis
473 and application of hybrid nanocrystals. Chemical Reviews, 120, 2123–2170.

474 Lu, L., Kobayashi, A., Kikkawa, Y., Tawa, K., and Ozaki, Y. (2006) Silver Nanoplates with
475 Special Shapes: Controlled Synthesis and Their Surface Plasmon Resonance and
476 Surface-Enhanced Raman Scattering Properties. Chemistry of Materials, 18, 4894–4901.

477 Mayne, R.G., McSween, H.Y., McCoy, T.J., & Gale, A. (2009) Petrology of the unbrecciated
478 eucrites. Geochimica et Cosmochimica Acta, 73, 794–819.

479 Min, N.B. (1992) Growth mechanisms in real crystals. Journal of Synthetic Crystals, 21, 217–
480 229.

481 Nanda, K.K., Sahu, S.N., and Behera, S.N. (2002) Liquid-drop model for the size-dependent
482 melting of low-dimensional systems. Physical Review, A66, 13208.

483 Nielsen, M.H., Aloni, S., and De Yoreo, J.J. (2014) In situ TEM imaging of $CaCO_3$ nucleation
484 reveals coexistence of direct and indirect pathways. Science, 345, 1158–1162.

485 Penn, R.L. (2004) Kinetics of Oriented Aggregation. Journal of Physical Chemistry B, 108,
486 12707–12712.

487 Penn, R.L., and Banfield, J.F. (1998) Imperfect oriented attachment: dislocation generation in
488 defect-free nanocrystals. Science 281, 969–971.

489 Petsev, D.N., Chen, K., Gliko, O., and Vekilov, P.G. (2003) Diffusion-limited kinetics of the
490 solution-solid phase transition of molecular substances. Proceedings of the National
491 Academy of Sciences of the U.S.A., 100, 792–796.

Rubie, D.C., Tsuchida, Y., Yagi, T., Utsumi, W., Kikegawa, T., Shimomura, O., and Brearley, A.J. (1990) An in situ X ray diffraction study of the kinetics of the Ni_2SiO_4 olivine-spinel transformation. Journal of Geophysical Research, 95, 15829–15844.

Stokes, R.J., and Evans, D.F. (1997) Fundamentals of Interfacial Engineering, 1 edn. VCH Publishers, New York.

Sunagawa, I. (2005) Crystals: Growth, morphology, and perfection, 1 edn. Cambridge University Press, New York.

Tomkins, A.G. (2009) What metal-troilite textures can tell us about post-impact metamorphism in chondrite meteorites. Meteoritics and Planetary Science, 44, 1133–1149.

Tsuchiyama, A., Osada, Y., Nakano, T., and Uesugi, K. (2004) Experimental reproduction of classic barred olivine chondrules: open-system behavior of chondrule formation. Geochimica et Cosmochimica Acta: Journal of the Geochemical Society and the Meteoritical Society, 68, 653–672.

Turnbull, D. (1956) Phase changes. Solid State Physics, 3, 225–306.

van Aken, P.A., and Liebscher, B. (2002) Quantification of ferrous/ferric ratios in minerals: new evaluation schemes of Fe $L_{2,3}$ electron energy-loss near-edge spectra. Physics and Chemistry of Minerals, 29, 188–200.

van Aken, P.A., Liebscher, B., and Styrsa, V.J. (1998) Quantitative determination of iron oxidation states in minerals using Fe $L_{2,3}$ -edge electron energy-loss near-edge structure spectroscopy. Physics and Chemistry of Minerals, 25, 323–327.

Weisberg, M.K. (1987) Barred olivine chondrules in ordinary chondrites. Journal of Geophysical Research, 92, E663–678.

Welsch, B., Hammer, J., and Hellebrand, E. (2014) Phosphorus zoning reveals dendritic architecture of olivine. Geology, 42, 867–870.

Xian, H.Y., Zhu, J.X., Yang, Y.P., Li, S., Lin, X.J., Xi, J.X., Xing, J.Q., Wu, X., Yang, H.M., Zhou, Q., Tsuchiyama, A., He, H.P., and Xu, Y.G. (2023) Ubiquitous and progressively increasing ferric Iron content on the Lunar surfaces revealed by Chang'e-5 samples.

520 Nature Astronomy, 7, 280–286.

521

522 Figure Captions

523 **Figure 1. Morphological characteristics of a cluster sampled from the CE5 lunar**
524 **surface regolith. (A-B)** SEM images of the sample. The olivine and glass rows are
525 marked by a red circle in (A). **(C)** HAADF-STEM image of an FIB section that was
526 cut from the location framed by a red square in (B). Olivine, chromite whiskers
527 (marked by red arrows), and nanospheres of troilite and $npFe^0$ dispersed in amorphous
528 materials are observed in the section. **(D)** The TEM image of the whisker structure
529 composed of $npFe^0$, troilite, and chromite with a base of olivine.

530 **Figure 2. Morphological and structural characteristics of the sample. (A)** Low
531 magnification TEM image of the sample section. **(B)** The enlarged TEM image of
532 square 1 in (A), showing the interface between olivine and chromite. **(C)** The enlarged
533 TEM image of square 2 in (A), showing the interfaces between chromite and troilite,
534 and between troilite and $npFe^0$ nanosphere. **(D-G)** The fast Fourier transform (FFT)
535 patterns of the four minerals in (B) and (C).

536 **Figure 3. Statistics of troilite and $npFe^0$ nanoparticle diameters in the melt (red**
537 **line) and those on the top of the whisker structure (black line).** Blue area presents
538 their concentrated range of particle diameter.

539 **Figure 4. Morphology and $Fe^{3+}/\sum Fe$ distribution of the whisker structure in the**
540 **sample. (A)** HAADF-STEM image of the whisker structure in the FIB section. Red

squares 1 and 2 frame the EELS mapping areas. **(B)** The mapping image of square 1, which shows a higher Fe^{3+} content in the glass surrounding the whisker (Glass A) and lower Fe^{3+} content in glass which is relatively far from the whisker (Glass B). The pseudo color is determined by the integrate intensity ratio of Fe-L_3 and Fe-L_2 edge [i.e., I(L_3)/(L_2)] of each EELS spectrum, with the color bar positioned on the lower right of the Fig. 4. Delineated by the boundary at I(L_3)/(L_2) = 1.7, the colors signify the absence of Fe^{3+} [I(L_3)/(L_2) ≤ 1.7] and the mixture of Fe^{2+} and Fe^{3+} [1.7 < I(L_3)/(L_2) < 3.0], respectively. The same in (D). **(C)** EELS spectra collected from Glass A and Glass B. **(D)** The mapping image of square 2, also showing a higher Fe^{3+} content in Glass A and a lower Fe^{3+} content in Glass B.

Figure 5. A compositional comparison between (A) the region near the olivine surface (Glass A) and (B) internal region of the olivine particle (Glass B). The inset with an enlarged image shows an obvious intensity difference of Cr-K peaks between A and B. The intensities of the Si peaks in the two patterns have been normalized to be equal for comparison.

Figure 6. Developing stages of the whisker structure. The process begins with the nucleation of $npFe^0$ **(A)**, troilite **(B)**, and troilite-iron **(C)** nanospheres in the impact-induced glass; then an oriented attachment between the assemblages and olivine **(D-E)** takes places, providing a high-energy plane for the growth of chromite **(F)** with Cr from both melt and olivine and Fe^{2+} from the melt. Thus, a whisker structure containing $npFe^0$, troilite, and chromite with a base of olivine **(G)** forms.

562 **Figure 7. Simulated surface energy evolution with chromite crystallizing on**
563 **olivine.** The whole progress is described in three stages, beginning with two particles
564 of olivine and troilite existing independently in the impact-induced melts (stage I).
565 Then an oriented attachment between two particles increases the total energy by $\Delta G1$
566 and forms the assemblages of troilite and olivine (stage II). When their attachment
567 accomplishes (i.e., the curve reaches to break A), chromite spontaneously occurs
568 because the activating energy of its crystallization is provided (stage III). The stages
569 are differentiated by the background color of the curve.

570

571 # Tables

572 **Table 1.** Chemical compositions of materials in Chang'e-5 sample from STEM-EDS
573 analysis.

material	chemical constituents (at.%)①										
	Na	**Mg**	**Al**	**Si**	**Ca**	**Ti**	**Cr**	**Mn**	**Fe**	**S**	**O**
olivine②	0.63	15.68	0.15	13.44	0.17	0.14	0.15	0.22	10.10	0.00	59.32
chromite	1.04	2.09	4.88	8.59	2.24	3.23	6.56	0.23	8.71	0.00	62.43
troilite	0.00	0.00	0.56	7.57	0.55	0.01	0.00	0.41	36.37	36.35	18.18
$npFe^0$	0.00	0.08	0.78	5.54	1.22	0.00	0.00	0.82	75.92	0.51	15.13
glass	1.06	1.55	6.36	18.84	5.00	0.81	0.01	0.07	2.53	0.01	63.63

①These data were the averages of the studied areas in EDS mappings.

②The EDS quantitative results of crystallines, especially of chromite, troilite and $npFe^0$, have the contribution of the silicate glass.

574

575 **Table 2.** Concentrations of Fe with different valences in the Chang'e-5 sample based
576 on EELS results.

zone	peak position of Fe L_3-edge (eV)	peak position of Fe L_2-edge (eV)	$Fe^{3+}/\sum Fe$ ratio①
olivine	709.15	721.80	bdl②
chromite	708.55	721.45	bdl
troilite	708.80	721.65	bdl
$npFe^0$	708.75	721.80	bdl
Glass A	710.95	723.55	~ 30%
Glass B	710.15	722.40	~ 10%

①The Fe^{2+} contents cannot be estimated directly. In the area without an occurrence of metallic iron, the ratio of $Fe^{2+}/\sum Fe$ can be acquired via extracting the Fe^{3+} content from the total Fe content (i.e., $Fe^{2+}/\sum Fe = 1 - Fe^{3+}/\sum Fe$).

② Bdl: below the detection limit. The same below.

577

578 **Table 3.** Unit cell parameters of mineral phases in the samples, acquired by electronic
579 diffraction patterns and fast Fourier transform results from HRTEM.

mineral	**crystal system**	***a* (Å)**	***b* (Å)**	***c* (Å)**	***α* (°)**	***β* (°)**	***γ* (°)**
$npFe^0$	isometric	2.08	2.08	2.08	90	90	90
troilite	isometric	5.20	5.20	5.20	90	90	90
chromite	isometric	9.72	9.72	9.72	90	90	90
olivine	orthorhombic	4.86	10.44	5.27	90	90	90

580

This is the peer-reviewed, final accepted version for American Mineralogist, published by the Mineralogical Society of America.
The published version is subject to change. Cite as Authors (Year) Title. American Mineralogist, in press.
DOI: https://doi.org/10.2138/am-2023-9214. http://www.minsocam.org/

Figure 1

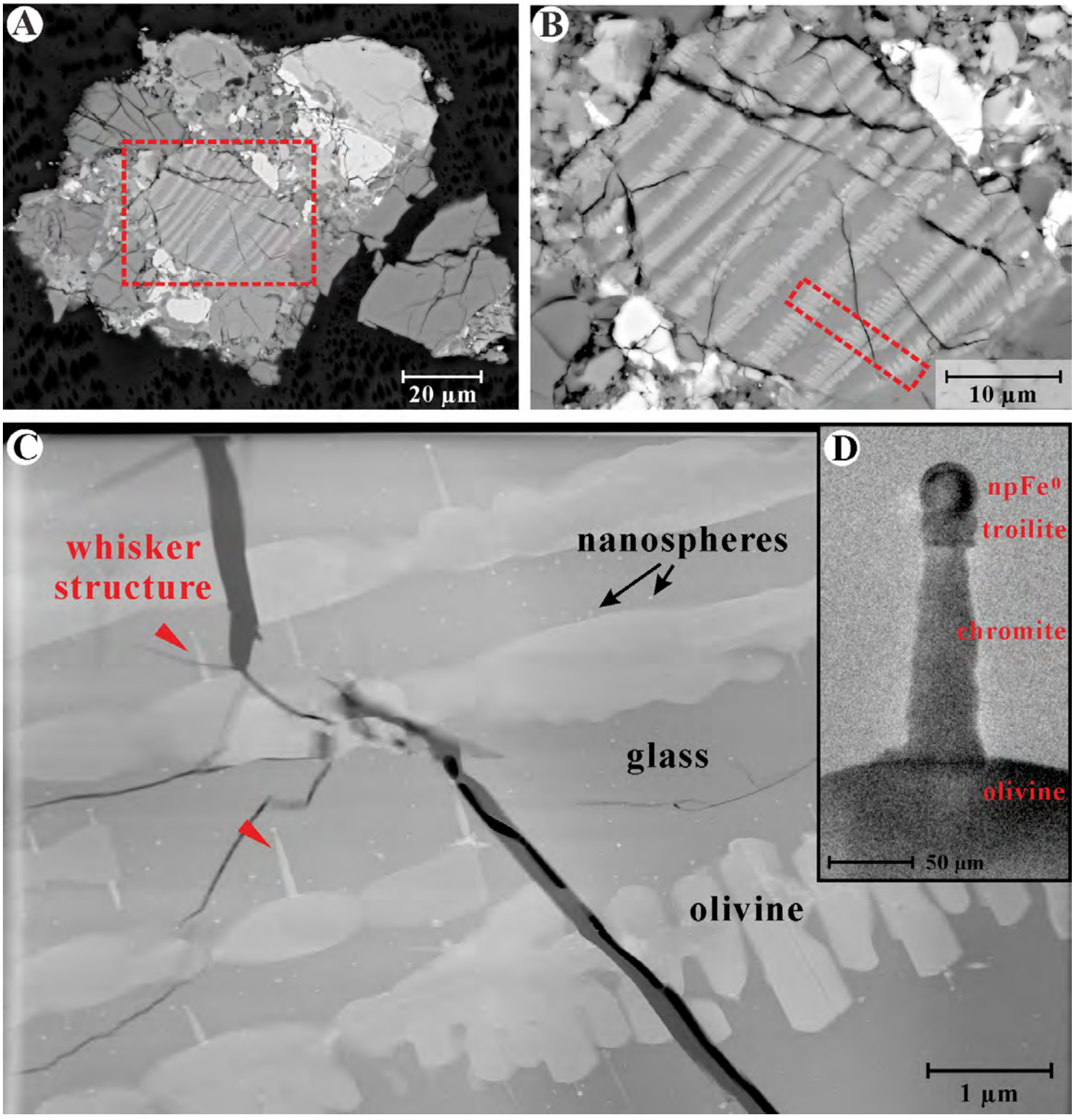

Figure 2

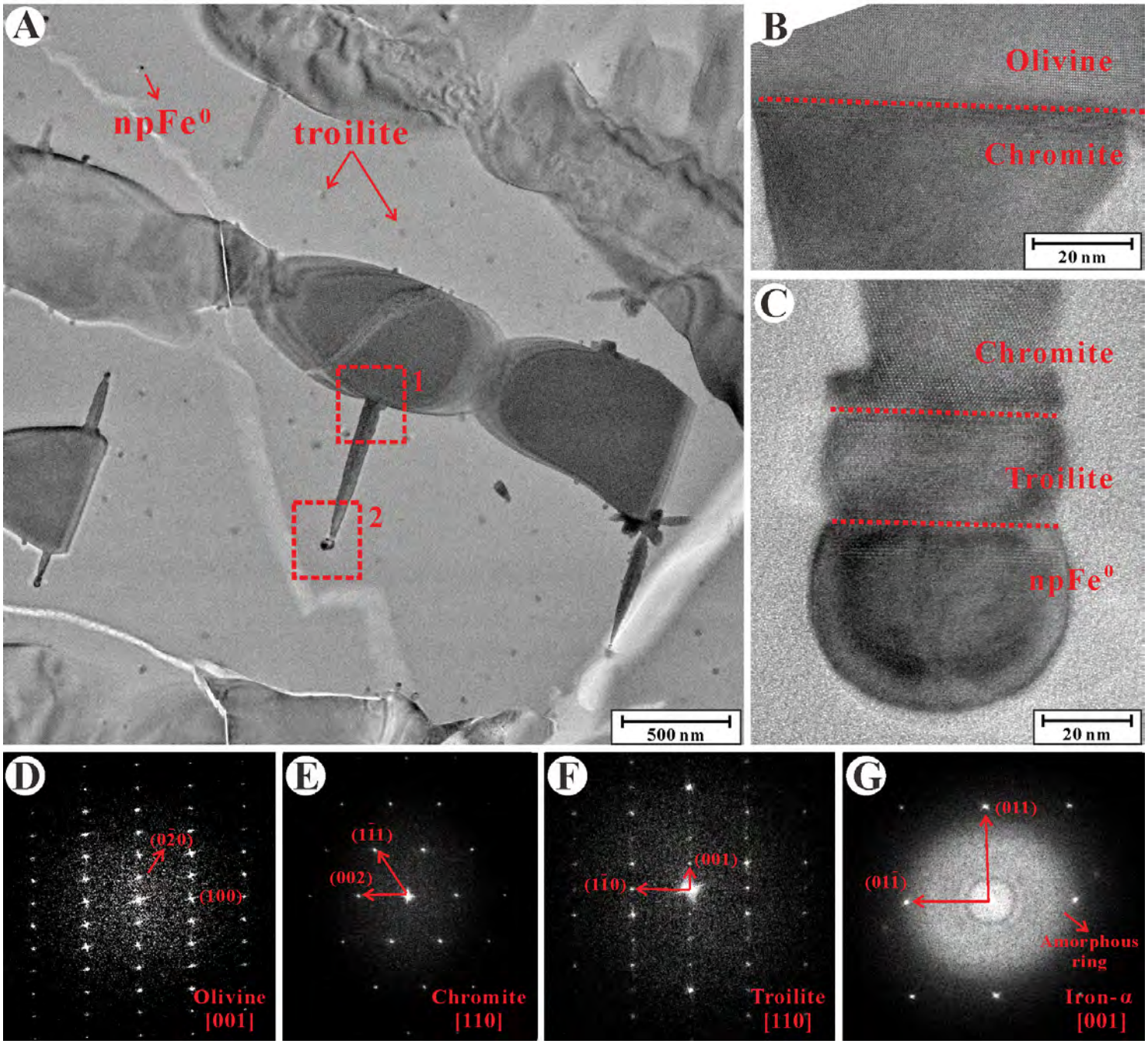

Figure 3

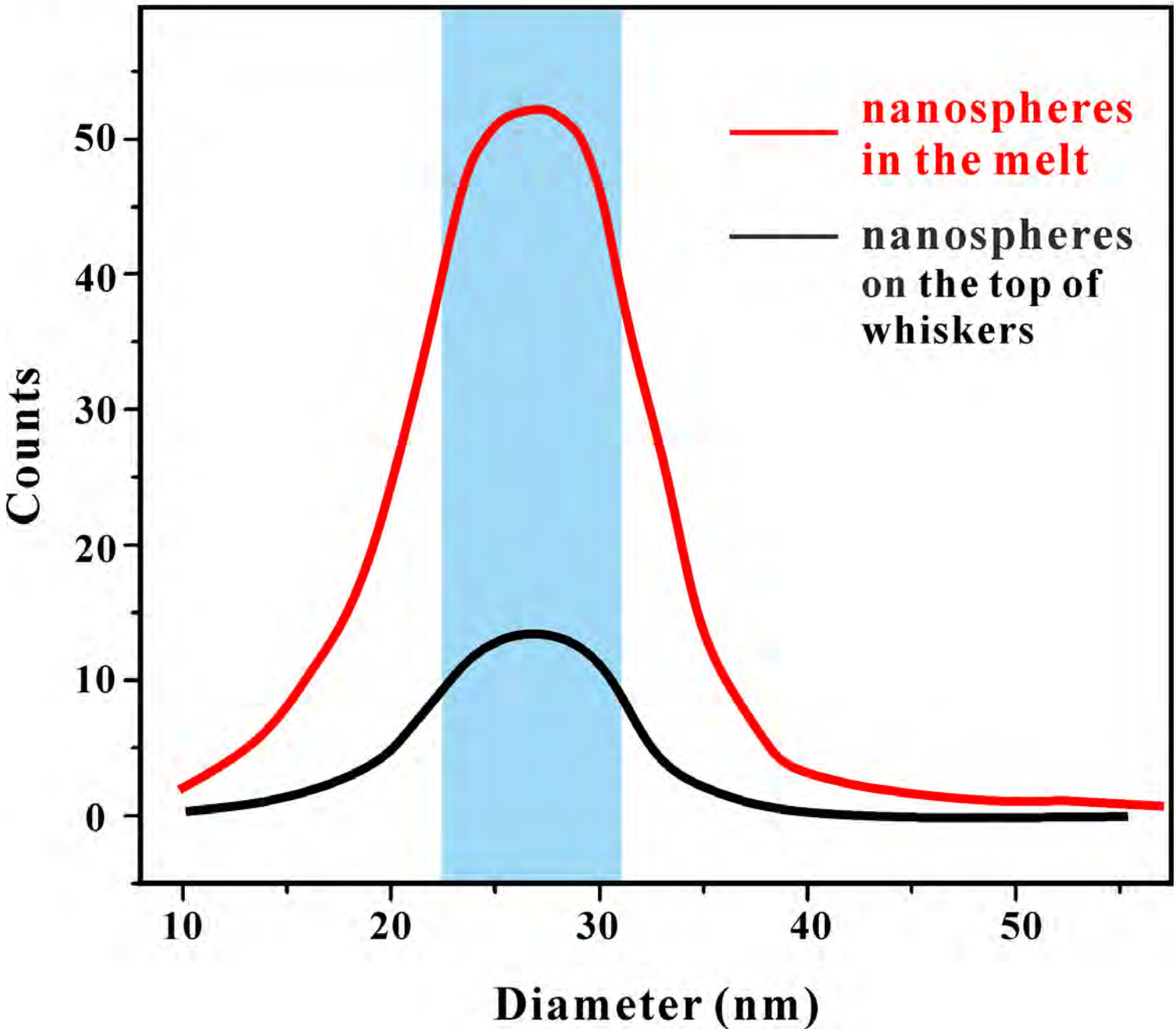

This is the peer-reviewed, final accepted version for American Mineralogist, published by the Mineralogical Society of America.
The published version is subject to change. Cite as Authors (Year) Title. American Mineralogist, in press.
DOI: https://doi.org/10.2138/am-2023-9214. http://www.minsocam.org/

Figure 4

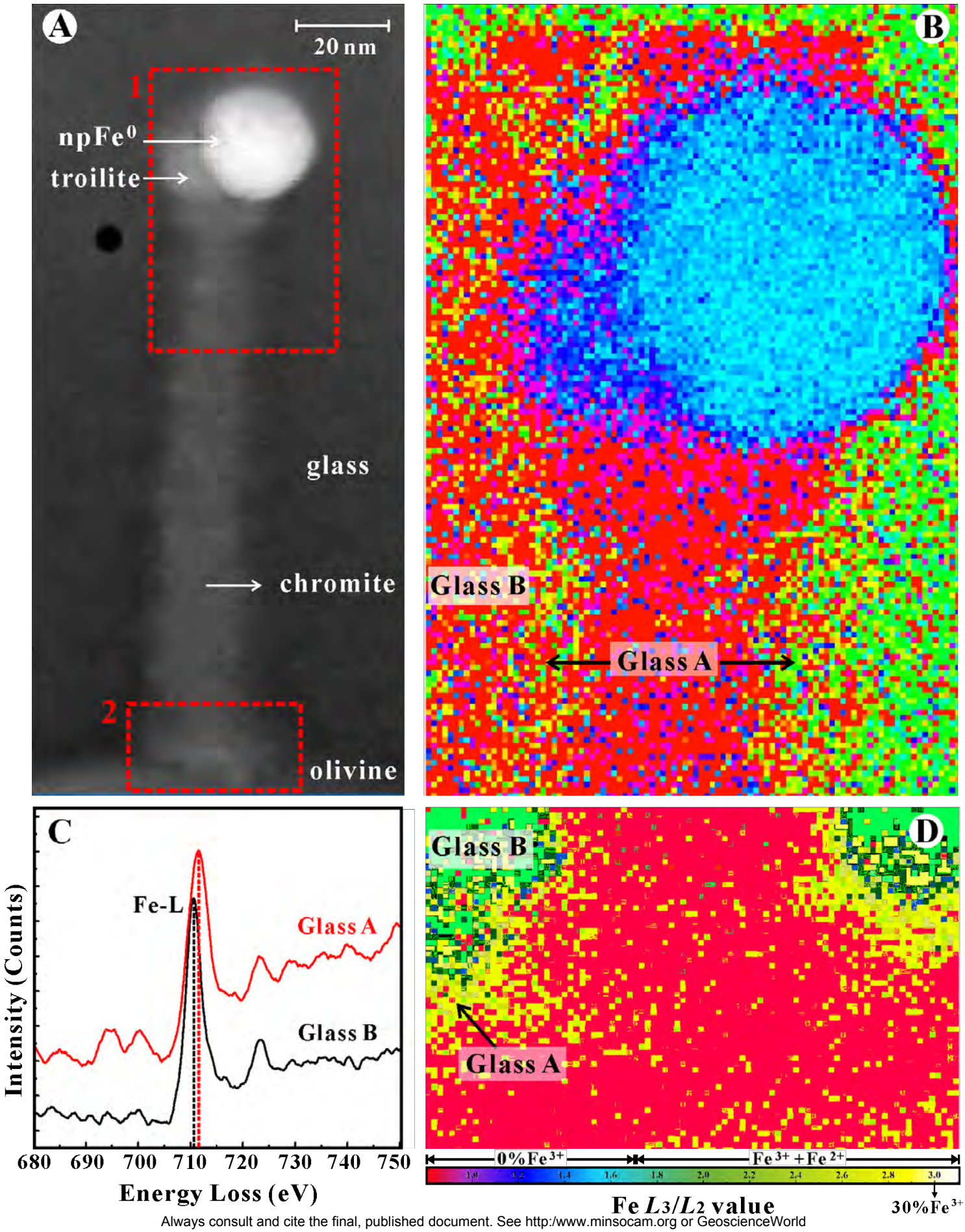

This is the peer-reviewed, final accepted version for American Mineralogist, published by the Mineralogical Society of America.
The published version is subject to change. Cite as Authors (Year) Title. American Mineralogist, in press.
DOI: https://doi.org/10.2138/am-2023-9214. http://www.minsocam.org/

Figure 5

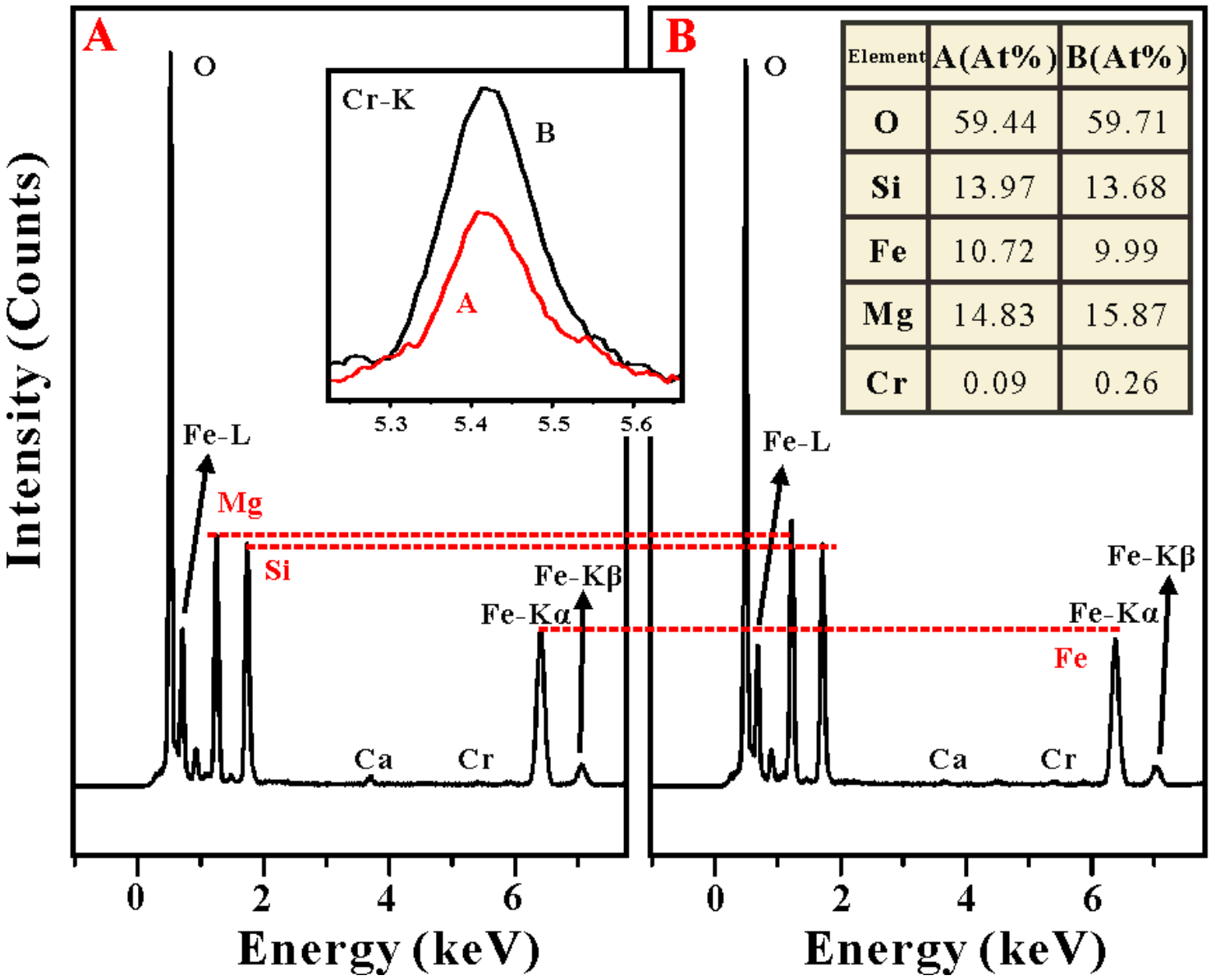

Element	A(At%)	B(At%)
O	59.44	59.71
Si	13.97	13.68
Fe	10.72	9.99
Mg	14.83	15.87
Cr	0.09	0.26

This is the peer-reviewed, final accepted version for American Mineralogist, published by the Mineralogical Society of America.
The published version is subject to change. Cite as Authors (Year) Title. American Mineralogist, in press.
DOI: https://doi.org/10.2138/am-2023-9214. http://www.minsocam.org/

Figure 6

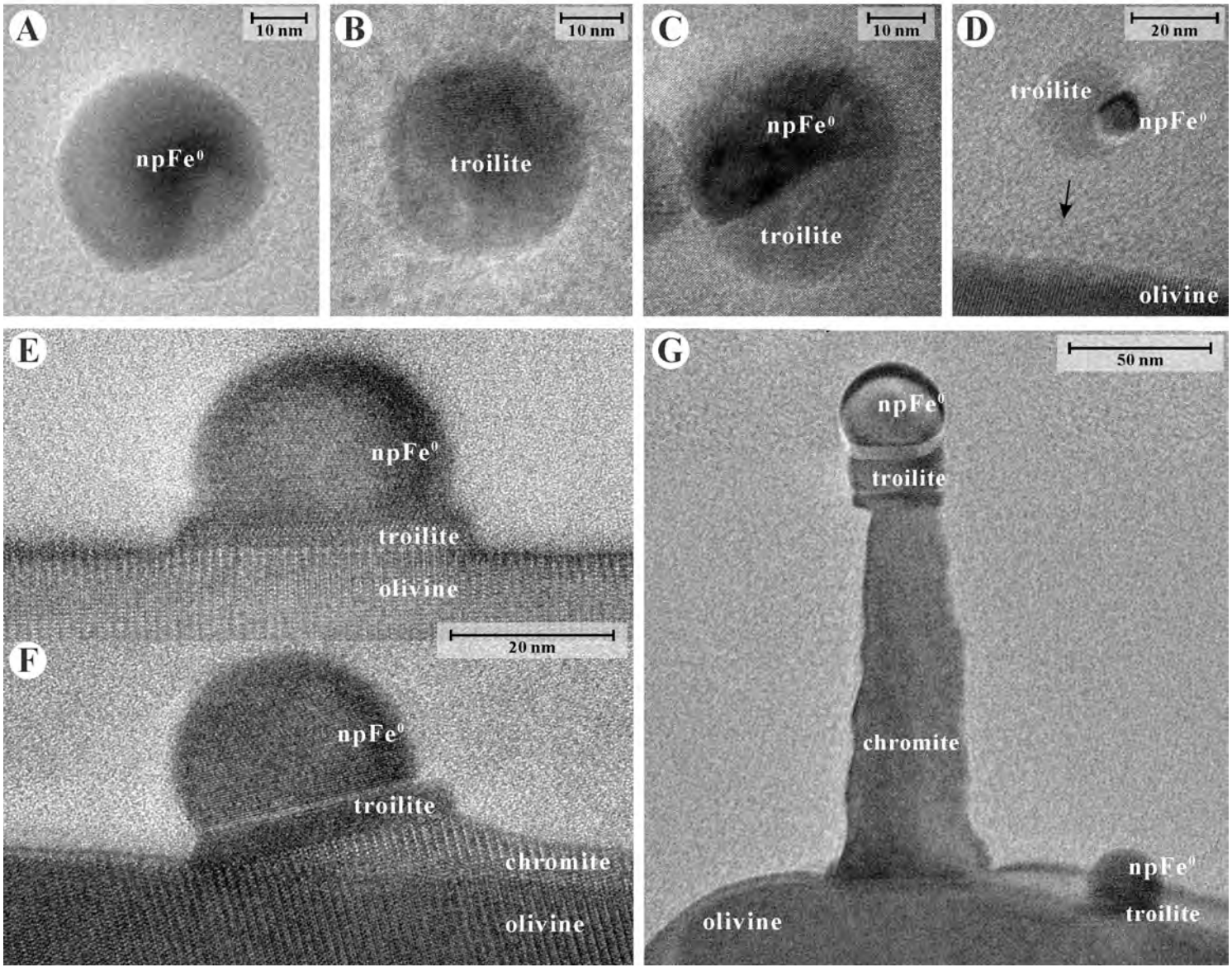

This is the peer-reviewed, final accepted version for American Mineralogist, published by the Mineralogical Society of America.
The published version is subject to change. Cite as Authors (Year) Title. American Mineralogist, in press.
DOI: https://doi.org/10.2138/am-2023-9214. http://www.minsocam.org/

Figure 7